



Chen, M., Zhang, B., Friedemann, S., Allegri, G., & Hallett, S. R. (2021). Effects of Ferromagnetic & Carbon-Fibre Z-Pins on the Magnetic Properties of Composites. *Composites Science and Technology*, 207, [108749].

<https://doi.org/10.1016/j.compscitech.2021.108749>

Peer reviewed version

License (if available):  
CC BY-NC-ND

Link to published version (if available):  
[10.1016/j.compscitech.2021.108749](https://doi.org/10.1016/j.compscitech.2021.108749)

[Link to publication record in Explore Bristol Research](#)  
PDF-document

This is the author accepted manuscript (AAM). The final published version (version of record) is available online via Elsevier at <https://doi.org/10.1016/j.compscitech.2021.108749> . Please refer to any applicable terms of use of the publisher.

## University of Bristol - Explore Bristol Research

### General rights

This document is made available in accordance with publisher policies. Please cite only the published version using the reference above. Full terms of use are available:  
<http://www.bristol.ac.uk/red/research-policy/pure/user-guides/ebr-terms/>

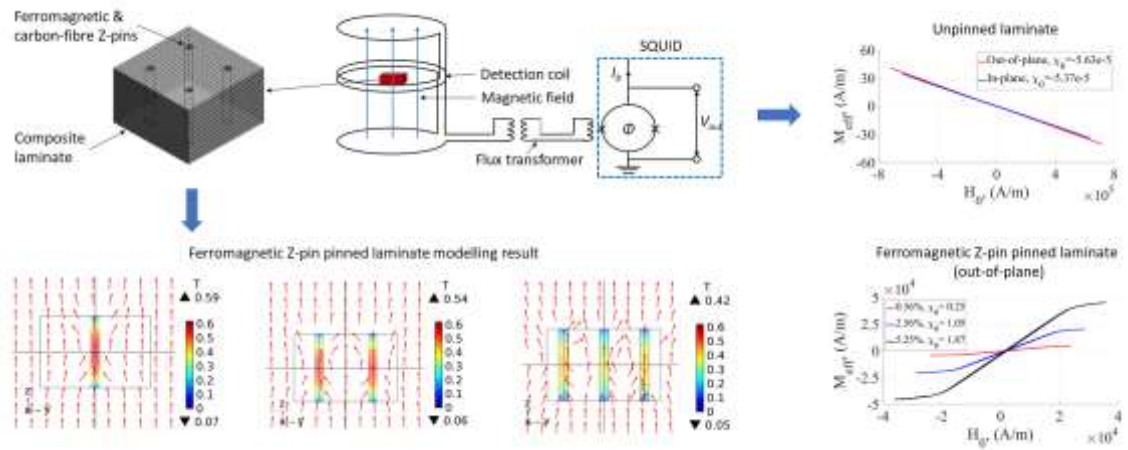
## Effects of Ferromagnetic & Carbon-Fibre Z-Pins on the Magnetic Properties of Composites

Mudan Chen<sup>a</sup>, Bing Zhang<sup>a,\*</sup>, Sven Friedemann<sup>b</sup>, Giuliano Allegri<sup>a</sup>, Stephen R. Hallett<sup>a</sup>

<sup>a</sup> *Bristol Composites Institute (ACCIS), University of Bristol, Bristol BS8 1TR, United Kingdom*

<sup>b</sup> *HH Wills Laboratory, University of Bristol, Bristol BS8 1TL, United Kingdom*

### Graphical Abstract



\*Corresponding author email address: [b.zhang@bristol.ac.uk](mailto:b.zhang@bristol.ac.uk) (Bing Zhang)

## **Effects of Ferromagnetic & Carbon-Fibre Z-Pins on the Magnetic Properties of Composites**

Mudan Chen<sup>a</sup>, Bing Zhang<sup>a,\*</sup>, Sven Friedemann<sup>b</sup>, Giuliano Allegri<sup>a</sup>, Stephen R. Hallett<sup>a</sup>

<sup>a</sup> *Bristol Composites Institute (ACCIS), University of Bristol, Bristol BS8 1TR, United Kingdom*

<sup>b</sup> *HH Wills Laboratory, University of Bristol, Bristol BS8 1TL, United Kingdom*

### **Abstract**

This paper investigates for the first time the effects of Z-pins on the magnetic properties of composite laminates. In-plane and out-of-plane M-H curves of IM7/8552 laminates with and without Z-pins have been characterised by an MPMS3 SQUID magnetometer. Two kinds of pin materials (T300/BMI composite and ferromagnetic Ni/Fe alloy) have been studied at three different volume fractions (nominally 0.5%, 2% and 4%). The unpinned and carbon-fibre pinned laminates were found to be diamagnetic. The carbon-fibre pin had no significant influence on the global magnetic properties of the laminates. The Ni/Fe alloy pin increased the laminate linear-part magnetic volume susceptibility up to 1.87 and 0.13 for the out-of-plane and in-plane directions, respectively. Numerical modelling has been conducted to support the investigation of the effect of the pin volume fraction on the overall magnetic susceptibility and saturation magnetisation. The laminate out-of-plane susceptibility exhibits a nonlinear behaviour dependent on pin volume fraction, due to interactions between adjacent pins. The saturation magnetisation is proportional to the pin volume fraction and independent of field direction.

**Keywords:** A. Multifunctional composites, A. Laminate, B. Magnetic properties, C. Finite Element Analysis (FEA), Z-pin

## 1 **1 Introduction**

2 Fibre-reinforced plastic (FRP) laminates have outstanding in-plane performance,  
3 but relatively weaker out-of-plane properties. Z-pinning has been developed as an  
4 effective through-thickness reinforcement (TTR) technology [1], along with stitching  
5 [2], tufting [3], 3D weaving [4], etc. A considerable amount of work has been reported  
6 in the literature regarding the mechanical reinforcement function of Z-pins [5–11]. More  
7 recently, there has been a strongly growing interest towards the exploration of multi-  
8 functionality in composites, in addition to load bearing functions. A number of studies  
9 have been published regarding the multi-functionality of Z-pinned composites [12–20].

10 Zhang et al. [12] characterised the Mode I & Mode II delamination self-sensing  
11 function of Z-pinned laminates by measuring the real-time through-thickness electrical  
12 resistance for both conductive and non-conductive fibre-reinforced plastics. They later  
13 extended the delamination monitoring method to composites reinforced by conductive  
14 Z-pin arrays and proposed a structural-level design strategy for multifunctional Z-  
15 pinned composites [13]. The latter is based on connecting Z-pins both in series and in  
16 parallel via arrays of electrodes attached to the laminate surface. Pegorin et al. [14]  
17 experimentally evaluated the effects of pin material (carbon FRP and metals) and  
18 volume content on the in-plane and through-thickness electrical conductivities at a  
19 coupon scale. It was found that the through-thickness conductivity linearly increased  
20 with pin volume content for all materials, and it was enhanced by a factor up to  $10^6$  by  
21 copper Z-pins with a volume fraction of 1.84%. Pegorin et al. [15] also proposed a  
22 Mode I delamination monitoring approach for laminates with Z-pin arrays. The  
23 electrical resistance between top and bottom electrodes that were attached in unpinned  
24 regions was found to increase with delamination length. Compared with unpinned

25 laminates, the resistance change of Z-pinned coupons due to delamination was much  
26 larger, thus potentially enabling a versatile and robust monitoring of in-service damage.  
27 Grigoriou et al. [16] later extended the electrical-based applications of Z-pins to  
28 sandwich composites. In the research of Kadlec et al. [17], Z-pins were found to  
29 effectively increase crack arrest ability of adhesive-bonded composite lap joints by 33%  
30 under static load. At the same time, the electrical resistance across pins was observed to  
31 have the same trend as crack growth, making this approach a promising candidate for  
32 structural health monitoring, thus supporting the certification of adhesive-bonded joints  
33 in aerospace applications.

34 By taking advantage of Z-pins combined with graphite sheets, Li et al. [18]  
35 developed a structure with a 3D enhanced thermal conductivity. It was found that 2.7%  
36 areal density of Z-pins enhanced the through-thickness and in-plane thermal  
37 conductivities by 215% and 115%, respectively, compared with unpinned graphite sheet  
38 composites. Through FE modelling, Pegorin et. al [19] found that the through-thickness  
39 thermal properties of Z-pinned composites could be tailored via pin volume fraction and  
40 the appropriate down-selection of pin materials, akin to the through-thickness electrical  
41 properties. With the pins acting as the thermal pathways, the through-thickness thermal  
42 conductivity grew linearly with pin content.

43 However, there is still a lack of studies regarding the effects of Z-pins on the  
44 magnetic properties of composites. Traditional FRP composites are magnetically inert:  
45 they do not show any remnant magnetism and only negligible enhancement of the  
46 relative magnetic permeability [21]. The weaker magnetic properties of composites  
47 compared to other materials represent an important limitation in several applications  
48 (e.g. in electromagnetic machines) [22,23]. For instance, the rotor containment sleeves

49 of a permanent magnet machine are normally made of carbon/glass FRP composites or  
50 weak-magnetic metals for load bearing. This generates a large non-magnetic gap  
51 between the stator and the magnet, significantly reducing the resulting electromagnetic  
52 force. Yon et al. [22] designed a magnetically semi-permeable sleeve to overcome this  
53 drawback. Based on an analytical model, they estimated that an optimum relative  
54 magnetic permeability ( $\mu_r = 7.2$ ) could increase the fundamental component of the air-  
55 gap flux density by 28%. A prototype machine with the sleeve made from cold-rolled  
56 304L stainless steel ( $\mu_r \approx 2$ ) was manufactured and tested. It showed a 20% increment of  
57 the electromotive force compared to the magnetically inert material. However, the  
58 stainless steel had a low resistivity and needed to be incorporated into a laminated  
59 assembly, making the manufacture complex and expensive. With the same purpose,  
60 Edwards et al. [23] incorporated magnetic particles into composites by employing  
61 epoxy resin film loaded with pure iron particles into laminates. By embedding one film  
62 between every adjacent ply (8 plies, 7 films), the predicted relative permeability was  
63 improved, whilst the ultimate tensile strength was reduced to 60%.

64 Besides electromagnetic machines, Etches et al. [24] demonstrated how tailoring  
65 the magnetic properties of composites can be potentially used for magnetic actuation of  
66 the trailing edge of a morphing aerofoil. Two magnetic materials (barium ferrite and  
67 ferrofluids) were separately embedded into hollow glass fibres. Due to the particle size  
68 and viscosity, the maximum achievable volume fraction of barium ferrite was only 3%.  
69 For ferrofluids, the filler volume fraction reached 30%. The ferrofluids-filled coupon  
70 was successfully actuated in an applied magnetic field.

71 Compared with the methods for improving the magnetic properties of composites  
72 reviewed above, Z-pinning offers a relatively wider material selection range, since Z-

73 pins can be in principle made of any material that can be processed into small rods.  
74 Similar to the research on electrical and thermal properties of Z-pinned composites in  
75 [12,14,18], this study also places emphasis on the effects of Z-pins on the global  
76 physical properties of composites. Meanwhile, some local meso-scale analyses are also  
77 presented to better understand the global effects observed. Specimen preparation and  
78 experimental set-up are introduced in Section 2 and Section 3. The magnetic properties  
79 of single Z-pins (not inserted into a composite laminate) are first characterised in  
80 Section 4. Experimental results for Z-pinned laminate samples are then presented in  
81 Section 5. The influence of pin misalignment and volume fraction on the magnetic  
82 susceptibilities of through-thickness reinforced composites in both the in-plane and out-  
83 of-plane directions are discussed in Section 6.

## 84 **2 Specimen preparation**

85 Metallic and carbon FRP Z-pins have been widely characterised for their  
86 mechanical performance in the literature. 0.25 mm diameter Ni80/Fe20 permalloy pins  
87 (from GoodFellow) and 0.28 mm diameter T300/BMI pins (from DPP BV) were  
88 considered in this study.

89 Z-pinned laminate specimens were manufactured employing 16 plies of Hexcel's  
90 IM7/8552 carbon/toughened-epoxy prepreg, with a stacking sequence of  $[0^\circ/+45^\circ/90^\circ/-$   
91  $45^\circ]_{2s}$ . This quasi-isotropic (QI) stacking sequence is a representative configuration for  
92 laminates in many structural applications. The maximum sample in-plane diagonal  
93 length allowed was 4.8 mm, due to the configuration of the sample holder in the  
94 MPMS3 magnetometer. Considering the pin spacing for nominal 0.5%, 2% and 4%  
95 volume fractions, the Z-pinned coupons were designed to have the dimensions of

96 3.1×3.1 ×2 mm. Figure 1 (a) shows the configuration of a 2% pinned coupon as an  
97 example.

98 The manufacturing process consisted of four steps. (1) The prepreg was defrosted  
99 for 2 hours and laid up to form the laminate, with de-bulking after every four plies. (2)  
100 The carbon-fibre pins were cut from a protruded rod stock and the alloy pins were cut  
101 from a wire roll with scissors; then both types of Z-pins were manually inserted into the  
102 uncured laminate. (3) The Z-pinned laminate was cured in an autoclave, following the  
103 cycle recommended by Hexcel [25]. (4) Finally, the coupons were carefully cut from  
104 the cured laminate using a water-cooled diamond-coated saw.

### 105 **3 Experimental set-up**

106 A SQUID (Superconducting Quantum Interference Device) magnetometer model  
107 MPMS3 manufactured by Quantum Design was used in DC scan mode in this research  
108 (Figure 1 (b)). The SQUID DC mode measures directly the magnetic flux of the sample  
109 utilizing the Josephson effect, which employs interference of the wave function around  
110 a superconducting loop where the magnetic flux of the sample is coupled in via a flux  
111 transformer. Usage of gradiometer coils removes the signal from the applied magnetic  
112 field, allowing to detect the magnetic flux from the sample as the sample is moved  
113 through the gradiometer. From the measurement of the flux as a function of position in  
114 the gradiometer, the magnetic moment of the sample is extracted using the MPMS3  
115 software calibrated on a palladium standard [26,27]. A simplified schematic of the  
116 measurement system is drawn in Figure 1 (c), with the SQUID highlighted in the dashed  
117 green box, in which  $I_b$  is the bias current,  $\Phi$  is the flux threading the SQUID, and  $V_{out}$  is  
118 the voltage responding to the flux. The magnetic field in the MPMS3 is generated by a  
119 superconducting electromagnet.



120 As shown in Figure 1 (b), the applied magnetic field was always in the vertical  
121 direction. For the axial direction tests, a single z-pin (not inserted into the composite)  
122 was glued on a quartz rod with a semicircle cross section and the pin axis was aligned  
123 with the magnetic field direction. For the radial and angled pin tests, due to the pin  
124 tending to align itself with the applied magnetic field, it was inserted into a fixed nylon  
125 holder, to eliminate any rotation. The magnetic field was along the pin radius direction  
126 for radial tests, and there was an angle between the magnetic field and pin axis for the  
127 angled pin tests.

128 The Z-pinned laminate coupons were glued onto the nylon support cylinder and  
129 put into a capsule. Nylon contributes a negligible background signal as its permeability  
130 deviates less than  $10^{-5}$  from that of free space [28], i.e.  $1 < \mu_r < 1 + 10^{-5}$ . The  
131 magnetic field was applied along the  $0^\circ$  ply fibre direction (X axis) for the in-plane  
132 measurements, whilst the magnetic field was along the specimen thickness direction (Z  
133 axis) for the out-of-plane measurements.

134 In order to get a full M-H loop, the applied magnetic field  $H_0$  was increased  
135 linearly from zero to a field  $H_{\max}$  sufficient to observe magnetisation saturation, then  
136 decreased to  $-H_{\max}$ , and finally brought back to  $H_{\max}$ . The total duration of one scan was  
137 1.5 to 2 hours. Each scan was repeated twice to ensure the reliability of data.

#### 138 **4 Single pin results**

139 In the experiments, the total magnetic moment of a sample was measured and  
140 converted into an effective magnetisation using the measured sample volume. All the  
141 M-H curves shown below present this effective magnetisation  $M_{\text{eff}}$  against the external  
142 field  $H_0$ . Note that the magnetisation is nonuniform inside the sample as we show later  
143 in detail in the simulations. The effective magnetic susceptibility  $\chi_0$  of the tested

144 samples is extracted from linear fitting in the low-field regime of the M-H curve. From  
145 this point, the low-field relative permeability is calculated as  $\mu_r = \chi_0 + 1$ .

#### 146 **4.1 Carbon-fibre FRP pins**

147 In the DC SQUID option, a resolution of  $10^{-9}$  A·m<sup>2</sup> is achieved by measuring a gel  
148 capsule in a straw with the standard setup. For an individual carbon pin with its small  
149 volume (diameter:  $d = 0.28$  mm, length:  $l = 4$  mm), however, the magnetic moment is  
150 too small to be detected. This is consistent with the expected magnetic moment  $m \approx$   
151  $7 \times 10^{-11}$  A·m<sup>2</sup> in a field of  $\mu_0 H_0 = 0.1$  T for a sample of this size containing pure  
152 graphite [29] .

#### 153 **4.2 Ni/Fe pins**

##### 154 **4.2.1 Susceptibility vs. length**

155 Firstly, the effect of cure on the Ni/Fe Z-pin magnetic properties can be ignored,  
156 which was confirmed by testing a pin before and after curing and observing that the  
157 resulting M-H curves were the same.

158 The intrinsic magnetic permeability of Ni80/Fe20 permalloy is quite high [30],  
159 however, in a finite size volume, the effects of demagnetisation give rise to a complex  
160 variation of magnetisation  $M$  across the volume and hence the magnetic moment has a  
161 non-linear dependence on magnetic field. In some limited cases, the demagnetizing  
162 factor  $N$  can be used to obtain the internal field  $H$  as  $H = H_0 - NM$ . As reported  
163 [31,32], the demagnetizing factor  $N$  of a cylinder is a complex function of the  
164 susceptibility and ratio of length to diameter as well as the orientation of the magnetic  
165 field. In small magnetic fields, a linear dependence can be approximated using the  
166 demagnetizing factor  $N$  depending on the sample shape and orientation in magnetic  
167 field only [33]. In this work the non-linear regime was also studied and finite element

168 analysis was used to model the behaviour of the samples, as analytical expressions are  
169 not available.

170 Since the Ni/Fe pin has a constant diameter of 0.25 mm, pins with lengths ranging  
171 from 1.5 to 4.1 mm in both the axial and radial directions were characterised. The  
172 experimental single-pin M-H curves are plotted in Figure 2 (a, b). The slightly  
173 horizontal offset of the M-H curves is most likely due to the remnant field in the  
174 superconducting magnet following previous measurements at large magnetic fields.

175 For both directions, the magnetisation initially increases linearly with the applied  
176 magnetic field  $H_0$ , then, following a nonlinear response stage, it quickly reaches  
177 saturation. The curves also reveal the very soft ferromagnetic behaviour of these  
178 permalloy pins, as they have narrow hysteresis loops with very small coercive field and  
179 remanence [30]. For the axial orientation, the slope of the low-field linear regime is  
180 larger for longer samples and the non-linear response is shifted to lower fields for longer  
181 samples, while the radial M-H behaviour is almost coincident for all samples. The  
182 saturation magnetisation  $M_s$  is independent of pin length for both directions.

183 For a quantitative analysis, the low-field susceptibilities are plotted against the pin  
184 length in Figure 2 (c, d). This shows that the susceptibility for axial field orientation  
185 increases linearly from 21 to 100 with the pin length growing from 1.5 to 4.1 mm.  
186 Conversely, the values for radial orientation of the field are much lower, having a mean  
187 value of 2.5. In the low-field limit, the magnetic behaviour of the alloy pins can be  
188 captured as that of a cylinder in an axial field with a demagnetizing factor, in agreement  
189 with the linear M-H curve seen in the measurements at low fields. The demagnetizing  
190 factor  $N_z$  decreases with the length to diameter ratio in agreement with the increased  
191 effective susceptibility found in these measurements [31,32]. At the same time, the

192 demagnetizing factor  $N_x$  relating with the radially applied magnetic field is much higher  
193 than  $N_z$  for a long thin cylinder [34] and relatively independent of the pin length, in  
194 agreement with the experimental results.

#### 195 **4.2.2 Susceptibility vs. inclination angle**

196 Since pin misalignment is a common and unavoidable manufacturing feature in Z-  
197 pinned laminates, the effect of the inclination angle  $\alpha$  (the angle between pin axis and  
198 magnetic field) is explored. The out-of-plane misalignment angle usually varies  
199 between  $5^\circ$  and  $20^\circ$  [35]. A 4.05 mm Ni/Fe pin was tested at pre-defined  $0^\circ$ ,  $20^\circ$ ,  $40^\circ$ ,  
200  $60^\circ$ ,  $70^\circ$  and  $90^\circ$  inclination angles with an accuracy of  $\pm 2^\circ$ .

201 The experimental M-H curves are plotted in Figure 3 (a). The curves show a  
202 decrease of the initial slope and increase of the saturation field as the inclination angle  
203 increases, whilst the saturation magnetisation remains independent on the angle. The  
204 calculated saturation flux density  $B_s$  is around 1.1 T, which is consistent with the data  
205 for 80% nickel permalloy from literature [30]. The low-field susceptibilities are  
206 extracted and plotted in Figure 3 (b) as a function of the inclination angle. A nonlinear  
207 decrease trend is observed as the inclination angle increases.

## 208 **5 Laminate results**

### 209 **5.1 Unpinned laminate**

210 The individual sample dimensions for the unpinned carbon fibre reinforced plastic  
211 (CFRP) coupons were  $3.2 \text{ mm} \times 3.1 \text{ mm} \times 2.0 \text{ mm}$ . Since the laminate has a quasi-  
212 isotropic stacking sequence, it is expected to exhibit negligible differences in magnetic  
213 properties for any arbitrary in-plane direction.

214 The out-of-plane and in-plane M-H curves of the unpinned specimen are plotted in  
215 Figure 4 (a). They present linear decreasing trends, and no saturation and hysteresis

216 were observed even at much higher  $H_{\max}$  values than those employed in the  
217 characterisation of alloy Z-pins. This confirms that the CFRP considered here is a  
218 weakly diamagnetic material [36]. The in-plane and out-of-plane M-H curves almost  
219 coincide, with susceptibility values of  $-5.37 \times 10^{-5}$  and  $-5.63 \times 10^{-5}$ , respectively.

## 220 **5.2 Carbon-fibre Z-pin pinned laminate**

221 Three carbon-fibre Z-pin pinned coupons with different pin volume fractions were  
222 tested. The actual volume fractions were calculated at 0.51%, 2.00% and 4.46%, by  
223 accurately measuring the specimen dimensions and the pin length (including the small  
224 amount of protruding top and bottom).

225 The in-plane and out-of-plane M-H curves are plotted in Figure 4 (b), with the  
226 corresponding susceptibilities  $\chi_0$  listed in the legend. Similar to the case of the unpinned  
227 CFRP, all curves present small monotonically decreasing trends, which implies that  
228 carbon Z-pinned laminates are also diamagnetic in both in-plane and out-of-plane  
229 directions. It appears that the absolute value of the susceptibility decreases with the pin  
230 volume fraction for both directions. The out-of-plane susceptibility is quite close to that  
231 of the in-plane direction. Compared with unpinned CFRP (i.e., comparing Figure 4 (a)  
232 and (b)), the carbon fibre Z-pin reinforced coupons present effective susceptibilities  
233 with the same order of magnitude as for unpinned CFRP. This proves that carbon fibre  
234 pins have no large influence on the global magnetic susceptibility of a CFRP laminate.

## 235 **5.3 Ni/Fe Z-pin pinned laminate**

236 The actual pin volume fractions for the samples reinforced with alloy pins were  
237 measured at 0.56%, 2.56% and 5.25%, respectively. The corresponding experimental  
238 M-H curves are plotted in Figure 4 (c, d). The curves have similar trends to those for the  
239 single Ni/Fe pin tests. The saturation magnetisation  $M_s$  increases with the pin volume

240 fraction for both in-plane and out-of-plane directions. Similar to the results on single  
 241 alloy pins,  $M_s$  is independent from the field direction for a given pin volume fraction  
 242 (i.e. comparing the same-colour curves in Figure 4 (c) and (d)).

243 As shown in the legends of Figure 4 (c, d), low-field effective susceptibilities in  
 244 the linear response region for the 0.56%, 2.56%, 5.25% pinned samples are 0.25, 1.05,  
 245 1.87 (out-of-plane) and 0.01, 0.07, 0.13 (in-plane), respectively. Compared with the  
 246 diamagnetic unpinned coupon, the laminate with Ni/Fe Z-pins become strongly  
 247 paramagnetic, with large susceptibilities. The low-field susceptibilities against pin  
 248 volume fractions are plotted with solid lines in Figure 4 (e) and (f). For comparison, the  
 249 dashed trend lines in Figure 4 (e) and (f) are given by the rule of mixtures:

$$250 \quad \chi_{0\_sample} = (1 - V_{f\_pin}) \cdot \chi_{0\_lam} + V_{f\_pin} \cdot \chi_{0\_pin} \quad (1)$$

251 where  $\chi_{0\_sample}$ ,  $\chi_{0\_lam}$  and  $\chi_{0\_pin}$  are the effective susceptibilities of pinned sample,  
 252 unpinned laminate, and pin, respectively.  $V_{f\_pin}$  is the pin volume fraction. Since  $\chi_{0\_lam}$   
 253 was measured to be very small for both directions (in the order of  $10^{-5}$ ),  $\chi_{0\_sample}$  is  
 254 dominated by the pin volume fraction and susceptibility. When considering the in-plane  
 255 behaviour, the experiments and analytical prediction agree well and only exhibit a slight  
 256 difference for the 2.56% volume fraction sample. However, the difference is more  
 257 evident for the out-of-plane direction especially at a higher pin volume fraction, which  
 258 means that the magnetic susceptibility of the pinned samples does not increase linearly  
 259 to the volume fraction of the soft-ferromagnetic through-thickness reinforcement. This  
 260 is potentially due to the pin misalignment and interaction, which will be further  
 261 investigated in the following section with the aid of finite element analysis (FEA).

## 262 **6 Discussion**

263 Comparing the test results for the unpinned laminate in Section 5.1 and the Ni/Fe  
264 Z-pinned laminate in Section 5.3, it can be concluded that the magnetic properties of a  
265 ferromagnetic pinned laminate are dominated by the pins. Since in Section 5.2 carbon-  
266 fibre pins have been shown to have minor influence on the global magnetic behaviour of  
267 composites, only the effects of Ni/Fe pins will be further discussed in this section,  
268 considering the effects of pin misalignment, interaction, and volume fraction.

### 269 **6.1 Pin misalignment effect**

270 As illustrated in the experiments, the saturation magnetisation  $M_s$  is independent  
271 of the inclination angle (Figure 3 (a)), and pin length (Figure 2 (a, b)). It has also been  
272 demonstrated in Figure 4 (c) and (d) that  $M_s$  increases with pin volume fraction. Thus,  
273  $M_s$  will also increase with pin misalignment since the latter leads to a larger pin volume  
274 fraction in a fixed thickness laminate with the pins running the full thickness.

275 The misalignment influences the low-field susceptibility of a Z-pinned laminate in  
276 four aspects. Firstly, the effective susceptibility of the laminate will increase due to the  
277 increased pin volume fraction caused by misalignment, similar to the saturation  
278 magnetisation discussed above. Secondly, the longer pin length due to misalignment  
279 will result in a change of the demagnetizing factor in a different way for in-plane and  
280 out-of-plane orientations. The growth of pin length due to misalignment results in an  
281 apparent increase of the effective susceptibility  $\chi_0$  of a single pin for the out-of-plane  
282 direction (Figure 2 (c)), while no obvious influence for the in-plane property (Figure 2  
283 (d)). Thirdly, the inclination angle due to pin misalignment has further effects on the  
284 demagnetizing factor as shown in Figure 3 (b). For misalignment angle typically within  
285  $20^\circ$  [35], it shows in Figure 3 (b) that the segment of  $0^\circ$  to  $20^\circ$  which corresponds to the

286 out-of-plane direction of Z-pinned laminate only slightly decreases, while the part from  
287 90°-70° related with the laminate in-plane direction has an apparent increment.  
288 Fourthly, pin misalignment would change the pin-to-pin distance in three dimensions  
289 and thus affect the pin interaction via magnetic field. A systematic study on the effect of  
290 pin misalignment will be addressed in a separate study by taking the aforementioned  
291 aspects into account.

## 292 **6.2 Pin volume fraction effect**

### 293 **6.2.1 Numerical modelling**

294 The commercial FEA tool COMSOL Multiphysics® was employed to help explain  
295 the influence of pin volume fraction. The magnetic vector potential  $\mathbf{A}$  is employed as a  
296 field variable for the element nodes in the FE models. The following equations are used  
297 for the magnetostatics case [37]:

$$298 \quad \nabla \cdot \mathbf{B} = 0 \quad (2)$$

$$299 \quad \mathbf{B} = \nabla \times \mathbf{A} \quad (3)$$

$$300 \quad \mathbf{B} = \mu_0(\mathbf{H} + \mathbf{M}) \quad (4)$$

301 where  $\mu_0$  is the vacuum permeability. The modelling strategy is verified through the  
302 alloy pin and pinned laminate tests as presented in Sections 4.2 and 5.3.

303 Each of the verification models consisted of the coupon (single pin or pinned  
304 laminate) in the middle of a relatively large free-space sphere and a layered infinite  
305 empty domain outside, as shown in Figure 5 by taking the 3 by 3 pin embedded  
306 laminate as an example. When modelling the tested Ni/Fe Z-pinned coupons, the pin  
307 misalignment must be considered since it affects the magnetic properties of composites  
308 as discussed in Section 6.1. To measure the pin misalignment, the sample top and  
309 bottom surfaces were scanned with a microscope, then each pin was located from the



310 scanned photos. Pin misalignment angles were determined by the distance between pin  
311 ends and sample edges. For the 1-pinned, 4-pinned and 9-pinned samples, the average  
312 misalignment angles are calculated as  $9.1^\circ$ ,  $8.4^\circ$ ,  $6.3^\circ$  respectively. Tetrahedral elements  
313 were employed throughout the whole mesh. For all the models presented here, mesh  
314 convergence studies have been conducted. There are 32 elements along the top or  
315 bottom circle and 16 elements per/mm in the length direction. A uniform background  
316 magnetic field was applied, which is consistent with the experimental set-up. The B-H  
317 curve of 80% nickel permalloy (Figure 6) from the COMSOL nonlinear magnetic  
318 material library [38] was used for the pin in the simulation. The material data in  
319 COMSOL originates from the MagWeb database [39].

320       The modelling verification results are presented in the supplementary material. It  
321 shows that good agreement between experimental measurements and modelling  
322 predictions is obtained, and minor discrepancies only arise in the transition region for  
323  $60^\circ$  and  $70^\circ$  angled pins. These differences could be attributed to the following factors.  
324 Firstly, the pins are modelled as a cylinder, while the real pin end shape is not perfectly  
325 flat after being cut with scissors. In addition, during the manufacturing process of wire  
326 such as pull-out, the grain texture inside the wire might be changed, which might  
327 influence the magnetic anisotropy and anisotropy of domain wall movements. Such  
328 magnetic anisotropy was not taken into account in the modelling. However, the overall  
329 simulation results are consistent with the experiments, especially for the most  
330 interesting linear and plateau regions of the response. The FEA also allows observing  
331 the flux density distribution inside pins, as shown in Figure 7 for the tested Ni/Fe Z-  
332 pinned coupons.

### 333 **6.2.2 Model results discussion**

334 In order to study the volume fraction effect, three ideal coupons (all having 3.1  
335  $\times 3.1 \times 2 \text{ mm}^3$  dimensions) respectively comprising 1, 4 and 9 pins were modelled with  
336 all the pins perfectly straight, without protruding parts.

337 The linear-region susceptibility versus pin volume fraction curves of the three  
338 models are plotted in Figure 8 (a, b). Similar with the experimental findings reported in  
339 Figure 4 (e, f), the out-of-plane curves from the simulations present a clearly nonlinear  
340 trend and it does not follow the rule of mixture in Figure 8 (a). On the other hand, the  
341 rule of mixture gives good results for the in-plane curves, as seen in Figure 8 (b).

342 To understand this, the cross-section flux distribution given in Figure 9 must be  
343 considered. For easy comparison, the colour bar ranges were set equal for each  
344 direction, and the maximum and minimum flux values are listed beside the triangle  
345 symbols in the graphs. For a single pin in the axial direction (out-of-plane), the flux is  
346 maximal at the pin centre (Figure 9 (a)) due to the focusing of flux by the high  
347 permeability of the material. In the radial direction, the flux is homogeneous over most  
348 of the pin with a small increase at the ends (Figure 9 (d)).

349 For multiple pins, the flux density from the external field is distributed over  
350 several pins and thus limits the enhancement of magnetisation compared to the case of a  
351 single pin. Furthermore, the extent of this flux sharing increases with the pin volume  
352 fraction and decreases with the pin spacing (comparing Figure 9 (b) and (c)). There are  
353 no observable interactions between pins when the magnetic field is applied transversely,  
354 and the flux density and distribution inside each pin show no significant dependence on  
355 pin volume fraction.

356 The saturation magnetisation  $M_s$  as a function of pin volume fraction is plotted in  
357 Figure 8 (c). This shows that the  $M_s$  is proportional to volume fraction for both  
358 directions and independent from the magnetic field direction, as the in-plane and out-of-  
359 plane curves completely coincide. This is simply because the pin volume fraction  
360 determines the number of atomic magnetic moments per unit volume. The observation  
361 also explains the experimental results for Ni/Fe pinned coupons reported in Section 5.3.

## 362 **7 Conclusions**

363 The magnetic properties of Z-pinned CFRP laminates have been investigated  
364 experimentally and numerically. Several conclusions could be drawn here:

365 1) Carbon-fibre Z-pins do not have large influence on the global magnetic  
366 properties of composites. 2) Soft ferromagnetic Ni/Fe Z-pins lead to a much larger  
367 magnetic susceptibility in the axial direction than in the radial one. 3) Ni/Fe pins  
368 enhance the laminate out-of-plane and in-plane low-field linear-region effective  
369 susceptibilities up to 1.87 and 0.13 at 5.25% volume fraction, respectively. 4) The low-  
370 field linear-region effective susceptibility of Ni/Fe pinned laminate increases with pin  
371 volume fraction nonlinearly due to pin interactions for the out-of-plane direction, but  
372 linearly for the in-plane orientation. 5) The global saturation magnetisation is only  
373 dependent on pin volume fraction and independent from field direction.

374 In summary, it is feasible to tailor the magnetic properties of composites through  
375 controlling the volume fraction of ferromagnetic pins. Embedding ferromagnetic  
376 through-thickness reinforcement in FRP laminates can widen the application range of  
377 FRP composites in electromagnetic applications.

## 378 **CRedit authorship contribution statement**

379 **Mudan Chen:** Methodology, Validation, Formal analysis, Investigation, Writing - Original Draft.

380 **Bing Zhang:** Conceptualization, Methodology, Validation, Formal analysis, Investigation, Resources,

381 Writing - Review & Editing, Supervision, Project administration. **Sven Friedemann**: Methodology,  
382 Validation, Formal analysis, Investigation, Resources, Writing - Review & Editing, Supervision.  
383 **Giuliano Allegri**: Conceptualization, Formal analysis, Writing - Review & Editing, Supervision.  
384 **Stephen R. Hallett**: Conceptualization, Formal analysis, Resources, Writing - Review & Editing,  
385 Supervision.

### 386 **Declaration of Competing Interest**

387 None

### 388 **Acknowledgements**

389 This work was supported by the Engineering and Physical Sciences Research  
390 Council (EPSRC) through the Centre for Doctoral Training in Advanced Composites  
391 for Innovation and Science (grant number EP/L016028/1). The COMSOL license was  
392 supported by the Bristol University CAME School Pump-Priming fund 2019. We are  
393 also grateful for advice given by Prof. Walther Schwarzacher and Dr Dmitry S. Ivanov  
394 on data analysis, Dr Chrystel Remillat, Dr Kate Gongadze and Dr Robert Hughes on  
395 simulations, as well as Mr Israel Osmond and Dr Mengze Zhu on experiments.

### 396 **References**

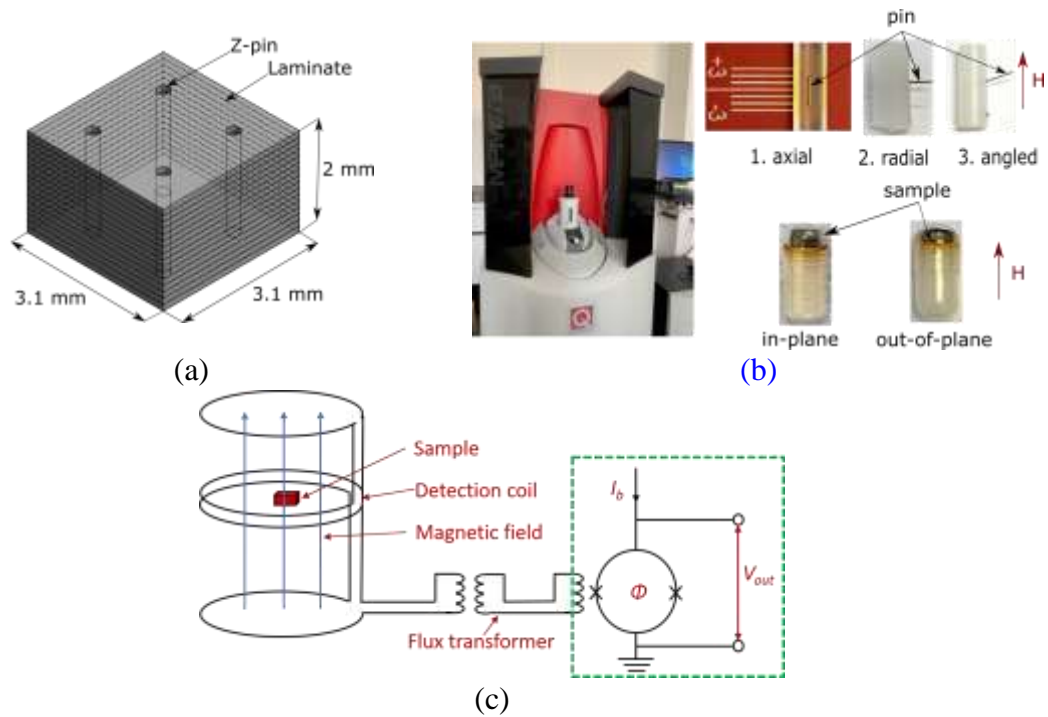
- 397 [1] A.P. Mouritz, Review of z-pinned laminates and sandwich composites,  
398 *Composites Part A: Applied Science and Manufacturing*. 139 (2020) 106128.  
399 <https://doi.org/10.1016/j.compositesa.2020.106128>.
- 400 [2] K. Dransfield, C. Baillie, Y.-W. Mai, Improving the delamination resistance of  
401 CFRP by stitching—a review, *Composites Science and Technology*. 50 (1994)  
402 305–317. [https://doi.org/10.1016/0266-3538\(94\)90019-1](https://doi.org/10.1016/0266-3538(94)90019-1).
- 403 [3] G. Dell’Anno, J.W.G. Treiber, I.K. Partridge, Manufacturing of composite parts  
404 reinforced through-thickness by tufting, *Robotics and Computer-Integrated  
405 Manufacturing*. 37 (2016) 262–272. <https://doi.org/10.1016/j.rcim.2015.04.004>.
- 406 [4] R. Gerlach, C.R. Siviour, J. Wiegand, N. Petrinic, In-plane and through-thickness  
407 properties, failure modes, damage and delamination in 3D woven carbon fibre  
408 composites subjected to impact loading, *Composites Science and Technology*. 72  
409 (2012) 397–411. <https://doi.org/10.1016/j.compscitech.2011.11.032>.
- 410 [5] F. Warzok, G. Allegri, M. Gude, S.R. Hallett, Experimental study of Z-pin fatigue;  
411 understanding of mode I and II coupon behaviour, *Composites Part A: Applied  
412 Science and Manufacturing*. 127 (2019) 105615.  
413 <https://doi.org/10.1016/j.compositesa.2019.105615>.

- 414 [6] A.R. Ravindran, R.B. Ladani, C.H. Wang, A.P. Mouritz, Hierarchical mode I and  
415 mode II interlaminar toughening of Z-pinned composites using 1D and 2D carbon  
416 nanofillers, *Composites Part A: Applied Science and Manufacturing*. 124 (2019)  
417 105470. <https://doi.org/10.1016/j.compositesa.2019.05.038>.
- 418 [7] M. Li, P. Chen, B. Kong, T. Peng, Z. Yao, X. Qiu, Influences of thickness ratios of  
419 flange and skin of composite T-joints on the reinforcement effect of Z-pin,  
420 *Composites Part B: Engineering*. 97 (2016) 216–225.  
421 <https://doi.org/10.1016/j.compositesb.2016.05.007>.
- 422 [8] F. Pegorin, K. Pingkarawat, S. Daynes, A.P. Mouritz, Influence of z-pin length on  
423 the delamination fracture toughness and fatigue resistance of pinned composites,  
424 *Composites Part B: Engineering*. 78 (2015) 298–307.  
425 <https://doi.org/10.1016/j.compositesb.2015.03.093>.
- 426 [9] H. Cui, M. Yasaee, A.R. Melro, Dynamic inter-fibre failure of unidirectional  
427 composite laminates with through-thickness reinforcement, *Composites Science  
428 and Technology*. 176 (2019) 64–71.  
429 <https://doi.org/10.1016/j.compscitech.2019.04.004>.
- 430 [10] B. M'membe, M. Yasaee, S.R. Hallett, I.K. Partridge, Effective use of metallic Z-  
431 pins for composites' through-thickness reinforcement, *Composites Science and  
432 Technology*. 175 (2019) 77–84.  
433 <https://doi.org/10.1016/j.compscitech.2019.02.024>.
- 434 [11] J. Hoffmann, G. Scharr, Compression properties of composite laminates reinforced  
435 with rectangular z-pins, *Composites Science and Technology*. 167 (2018) 463–  
436 469. <https://doi.org/10.1016/j.compscitech.2018.08.042>.
- 437 [12] B. Zhang, G. Allegri, M. Yasaee, S.R.R. Hallett, I.K.K. Partridge, On the  
438 delamination self-sensing function of Z-pinned composite laminates, *Composites  
439 Science and Technology*. 128 (2016) 138–146.  
440 <https://doi.org/10.1016/j.compscitech.2016.03.019>.
- 441 [13] B. Zhang, G. Allegri, S.R. Hallett, An experimental investigation into multi-  
442 functional Z-pinned composite laminates, *Materials and Design*. 108 (2016) 679–  
443 688. <https://doi.org/10.1016/j.matdes.2016.07.035>.
- 444 [14] F. Pegorin, K. Pingkarawat, A.P. Mouritz, Controlling the electrical conductivity  
445 of fibre-polymer composites using z-pins, *Composites Science and Technology*.  
446 150 (2017) 167–173. <https://doi.org/10.1016/j.compscitech.2017.07.018>.
- 447 [15] F. Pegorin, K. Pingkarawat, A.P. Mouritz, Electrical-based delamination crack  
448 monitoring in composites using z-pins, *Composites Part A: Applied Science and  
449 Manufacturing*. 104 (2018) 120–128.  
450 <https://doi.org/10.1016/j.compositesa.2017.10.025>.
- 451 [16] K. Grigoriou, R.B. Ladani, A.P. Mouritz, Electrical properties of multifunctional  
452 Z-pinned sandwich composites, *Composites Science and Technology*. 170 (2019)  
453 60–69. <https://doi.org/10.1016/j.compscitech.2018.11.030>.
- 454 [17] M. Kadlec, R. Růžek, P. Bělský, Concurrent use of Z-pins for crack arrest and  
455 structural health monitoring in adhesive-bonded composite lap joints, *Composites  
456 Science and Technology*. 188 (2020) 107967.  
457 <https://doi.org/10.1016/J.COMPSCITECH.2019.107967>.
- 458 [18] M. Li, Z. Fang, S. Wang, Y. Gu, Y. Li, Z. Zhang, Thermal conductivity  
459 enhancement and heat transport mechanism of carbon fiber z-pin graphite  
460 composite structures, *Composites Part B: Engineering*. 172 (2019) 603–611.  
461 <https://doi.org/10.1016/J.COMPOSITESB.2019.05.092>.

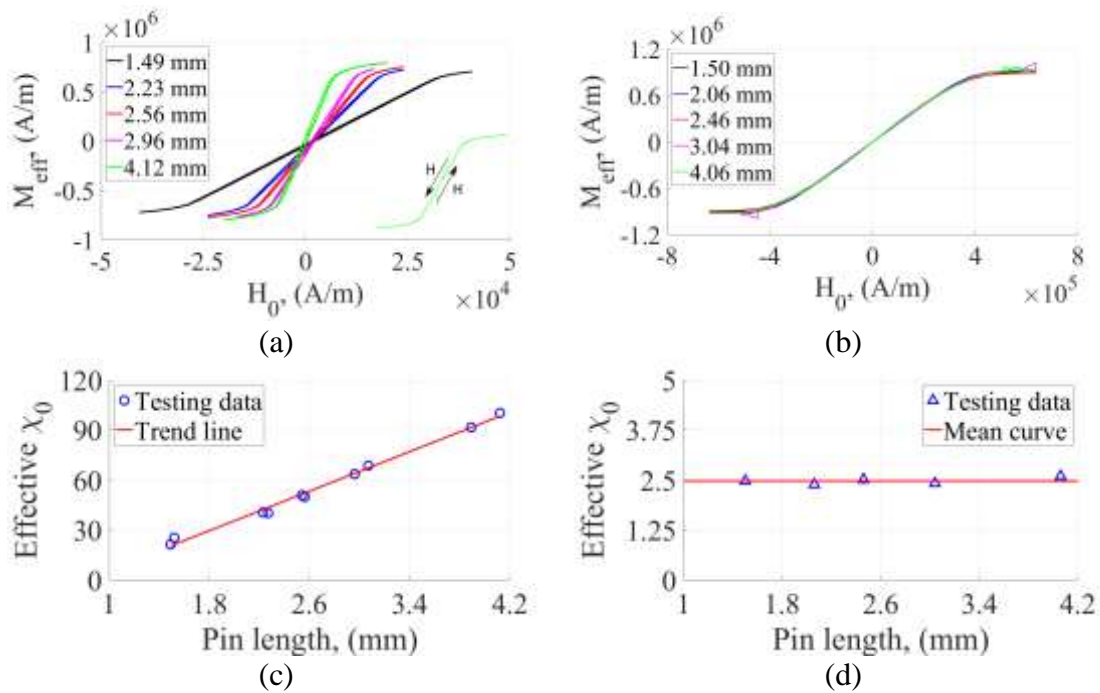
- 462 [19] F. Pegorin, K. Pingkarawat, A.P. Mouritz, Numerical analysis of the heat transfer  
463 properties of z-pinned composites, *Composites Communications*. 8 (2018) 14–18.  
464 <https://doi.org/10.1016/j.coco.2018.03.002>.
- 465 [20] B. Gu, H. Zhang, B. Wang, S. Zhang, X. Feng, Fracture toughness of laminates  
466 reinforced by piezoelectric z-pins, *Theoretical and Applied Fracture Mechanics*. 77  
467 (2015) 35–40. <https://doi.org/10.1016/j.tafmec.2015.01.007>.
- 468 [21] J. Summerscales, *Microstructural Characterisation of Fibre-Reinforced*  
469 *Composites*, Woodhead Publishing, 1998.
- 470 [22] J.M. Yon, P.H. Mellor, R. Wrobel, J.D. Booker, S.G. Burrow, Analysis of  
471 semipermeable containment sleeve technology for high-speed permanent magnet  
472 machines, *IEEE Transactions on Energy Conversion*. 27 (2012) 646–653.  
473 <https://doi.org/10.1109/TEC.2012.2202232>.
- 474 [23] L.E. Edwards, J.M. Yon, I.P. Bond, P.H. Mellor, Structural magnetic composites  
475 for use in electro-mechanical applications, *ICCM International Conferences on*  
476 *Composite Materials*. 2015-July (2015) 19–24.
- 477 [24] J. Etches, I. Bond, P. Mellor, Manufacture and applications of magnetically active  
478 fibre reinforced composites, *Smart Mater. Struct.* 15 (2006) 288–294.  
479 <https://doi.org/10.1088/0964-1726/15/2/007>.
- 480 [25] Prepreg Data Sheet | Hexcel, (2020). <https://www.hexcel.com>.
- 481 [26] Magnetic Property Measurement System, MPMS 3 User’s Manual, (2016).
- 482 [27] M. Schmelz, R. Stolz, Superconducting Quantum Interference Device (SQUID)  
483 Magnetometers, in: A. Grosz, M.J. Haji-Sheikh, S.C. Mukhopadhyay (Eds.), *High*  
484 *Sensitivity Magnetometers*, Springer International Publishing, Cham, 2017: pp.  
485 279–311. [https://doi.org/10.1007/978-3-319-34070-8\\_10](https://doi.org/10.1007/978-3-319-34070-8_10).
- 486 [28] S. Hwang, S.-K. Lee, Efficient Experimental Design for Measuring Magnetic  
487 Susceptibility of Arbitrarily Shaped Materials by MRI, *Investigative Magnetic*  
488 *Resonance Imaging*. 22 (2018) 141–149.  
489 <https://doi.org/10.13104/imri.2018.22.3.141>.
- 490 [29] J. Heremans, C.H. Olk, D.T. Morelli, Magnetic susceptibility of carbon structures,  
491 *Phys. Rev. B*. 49 (1994) 15122–15125.  
492 <https://doi.org/10.1103/PhysRevB.49.15122>.
- 493 [30] D. Jiles, *Introduction to Magnetism and Magnetic Materials*, CRC Press, 2015.
- 494 [31] D.-X. Chen, J.A. Brug, R.B. Goldfarb, Demagnetizing factors for cylinders, *IEEE*  
495 *Transactions on Magnetics*. 27 (1991) 3601–3619.  
496 <https://doi.org/10.1109/20.102932>.
- 497 [32] D.-X. Chen, E. Pardo, A. Sanchez, Fluxmetric and magnetometric demagnetizing  
498 factors for cylinders, *Journal of Magnetism and Magnetic Materials*. 306 (2006)  
499 135–146. <https://doi.org/10.1016/j.jmmm.2006.02.235>.
- 500 [33] X.B. Xu, L. Zeng, Ferromagnetic cylinders in earth’s magnetic field—a two-  
501 dimensional model of magnetizaion of submarine, (1998) 17.
- 502 [34] M. Sato, Y. Ishii, Simple and approximate expressions of demagnetizing factors of  
503 uniformly magnetized rectangular rod and cylinder, *Journal of Applied Physics*. 66  
504 (1989) 983–985. <https://doi.org/10.1063/1.343481>.
- 505 [35] M. Yasae, J.K. Lander, G. Allegri, S.R. Hallett, Experimental characterisation of  
506 mixed mode traction–displacement relationships for a single carbon composite Z-  
507 pin, *Composites Science and Technology*. 94 (2014) 123–131.  
508 <https://doi.org/10.1016/j.compscitech.2014.02.001>.

- 509 [36] A. Galehdar, K.J. Nicholson, P.J. Callus, W.S.T. Rowe, S. John, C.H. Wang, K.  
510 Ghorbani, The strong diamagnetic behaviour of unidirectional carbon fiber  
511 reinforced polymer laminates, *Journal of Applied Physics*. 112 (2012) 113921.  
512 <https://doi.org/10.1063/1.4764041>.
- 513 [37] R. Prozorov, V.G. Kogan, Effective Demagnetizing Factors of Diamagnetic  
514 Samples of Various Shapes, *Physical Review Applied*. 10 (2018) 1.  
515 <https://doi.org/10.1103/PhysRevApplied.10.014030>.
- 516 [38] Multiphysics Simulations Material Library - Adding Material Properties, (2021).  
517 <https://www.comsol.com/material-library>.
- 518 [39] Nickel Steel, MAGWEB. (2021). <https://magweb.us/product/nickel-steel/>.  
519

520

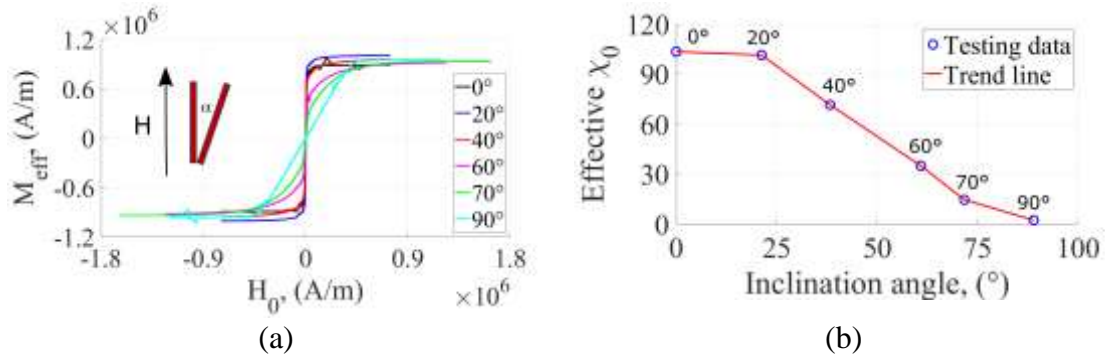


521 Figure 1. (a) Nominal 2% Z-pinned coupon configuration, (b) SQUID MPMS3  
 522 and sample installations, (c) schematic of the SQUID detecting system diagram.

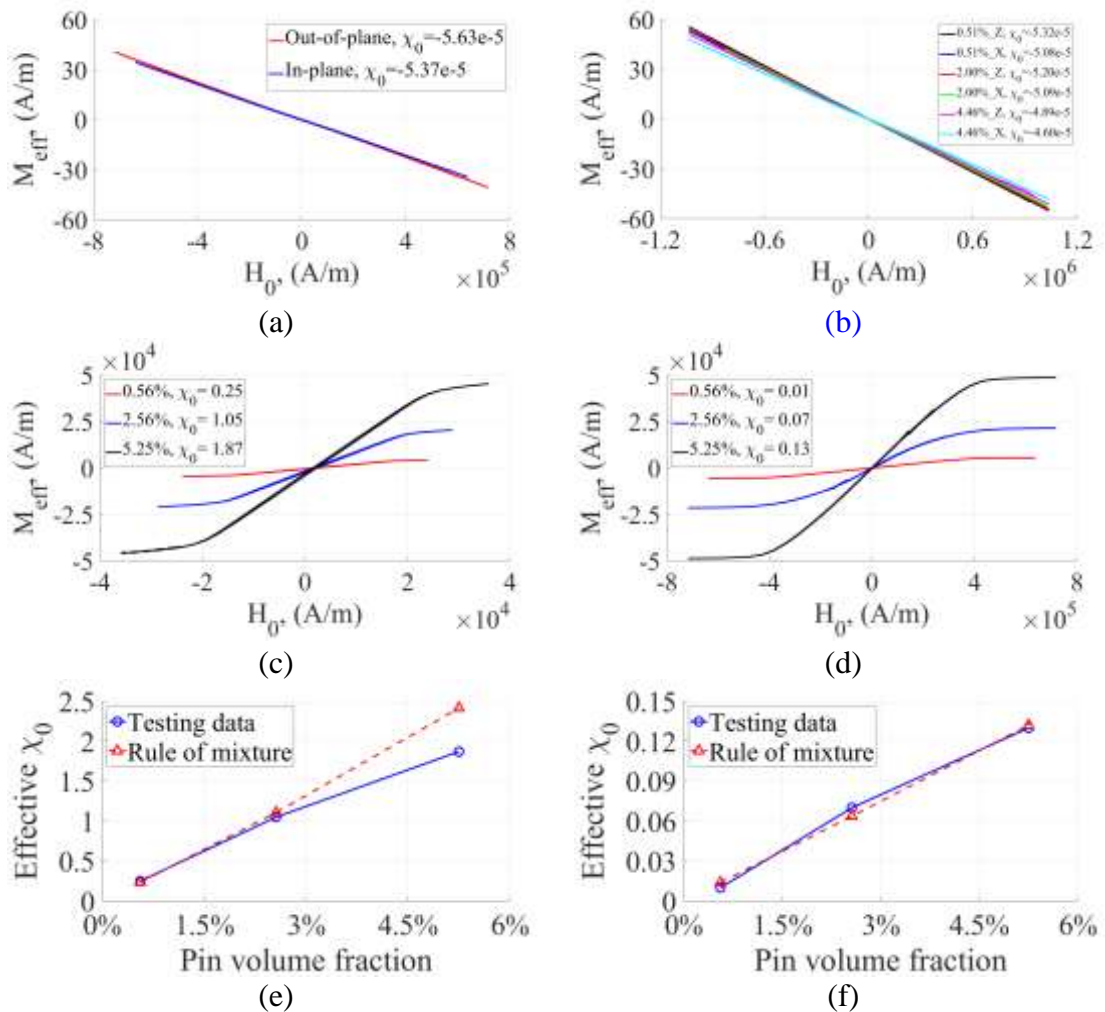


523 Figure 2. Ni/Fe pin experimental results: (a) axial M-H curves, (b) radial M-H  
 524 curves, (c) axial linear-part effective susceptibility against pin length, (d) radial linear-  
 525 part effective susceptibility against pin length.



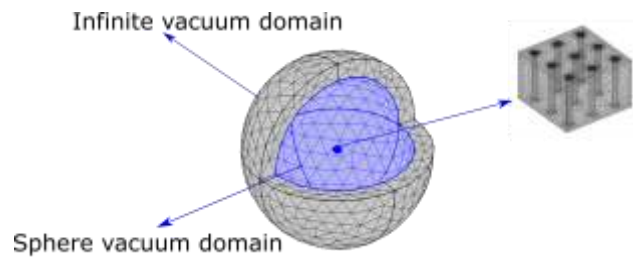


526 Figure 3. Misaligned Ni/Fe pin experimental results: (a) M-H curves, (b) linear-  
527 part effective susceptibility against inclination angle.



528 Figure 4. (a) M-H curves of the unpinned sample, (b) M-H curves of carbon FRP  
529 Z-pinned samples (out-of-plane: Z, in-plane: X); Ni/Fe Z-pinned samples M-H curves:  
530 (c) out-of-plane, (d) in-plane; linear-part effective magnetic susceptibility against the  
531 Ni/Fe pin volume fraction: (e) out-of-plane, (f) in-plane

532



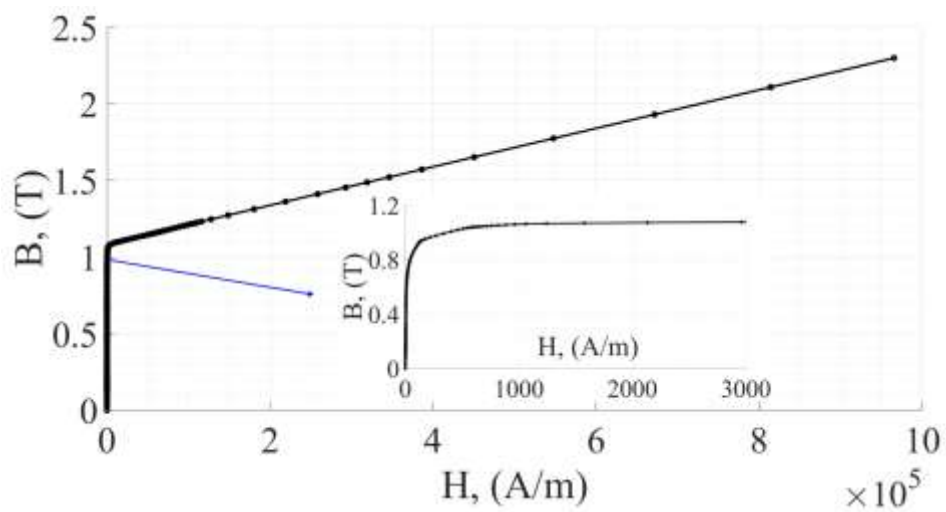
533 Figure 5. FEA model configuration and meshes (A quarter of the model is hidden

534 to make the inner geometry visible).

535

536

537



538

539 Figure 6. Permalloy B-H curve from the COMSOL material library [38,39].

540

541

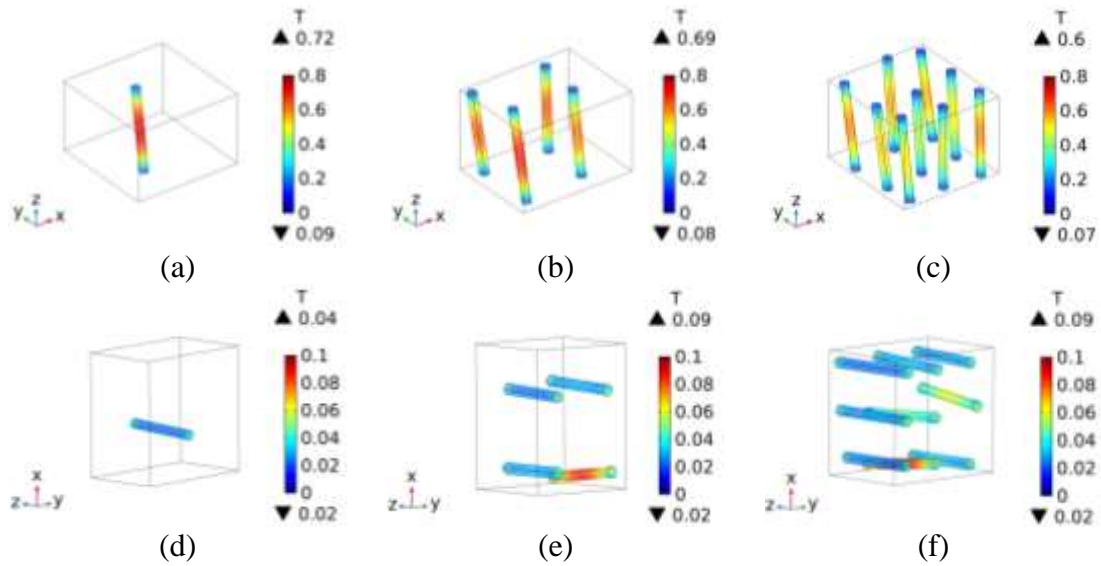
542

543

544

545

546

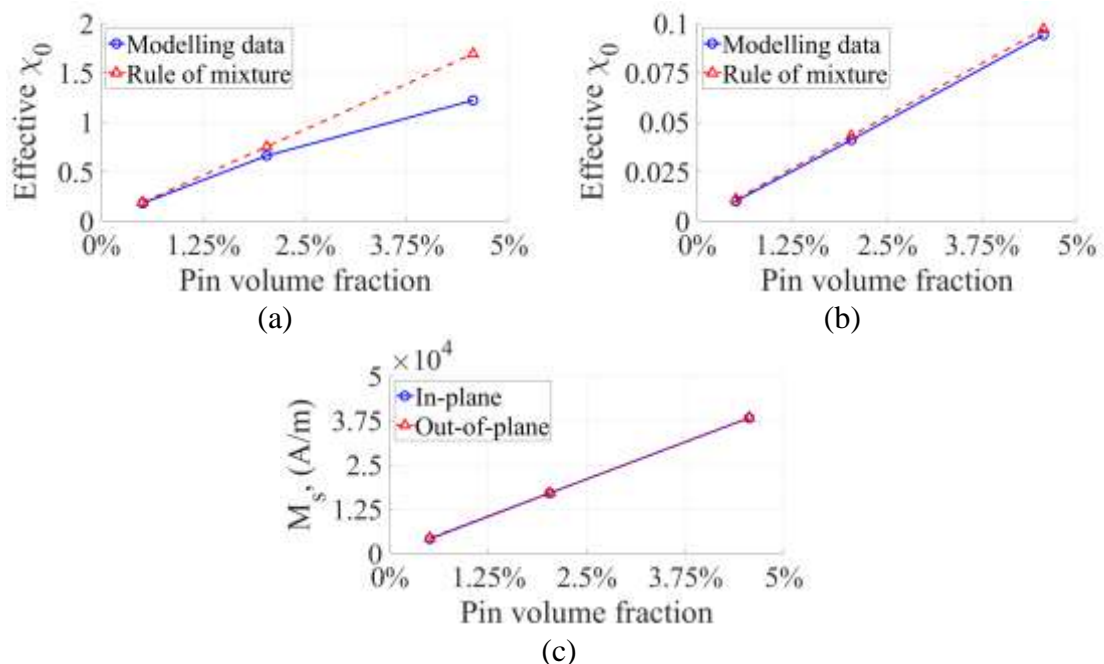


547 Figure 7. Flux density norm of Ni/Fe Z-pinned samples with 10000 A/m magnetic

548 field applied: (a-c) out-of-plane (d-f) in-plane.

549

550

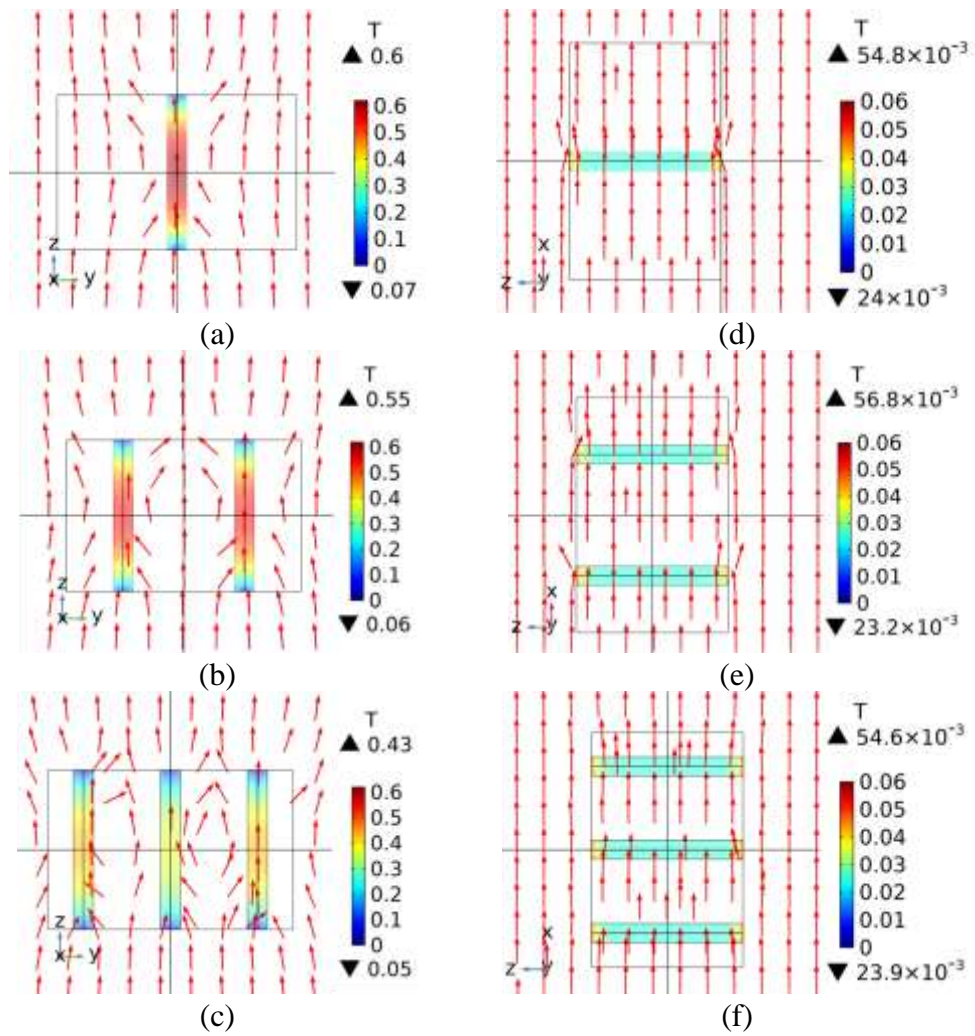


551 Figure 8. Modelling result of ideal Ni/Fe Z-pinned samples: (a) out-of-plane

552 linear-part effective magnetic susceptibility against pin volume fraction, (b) in-plane

553 linear-part effective magnetic susceptibility against pin volume fraction, (c) saturation

554 magnetisation against pin volume fraction.



555 Figure 9. Cross section flux density norm of pins and distribution around them  
 556 (modelling result of three ideal Ni/Fe Z-pinned samples with the 10000 A/m magnetic  
 557 field applied): (a-c) out-of-plane (d-f) in-plane.

558

559

560

Supplementary document

Mudan Chen, Bing Zhang, Sven Friedemann, Giuliano Allegri, Stephen R. Hallett

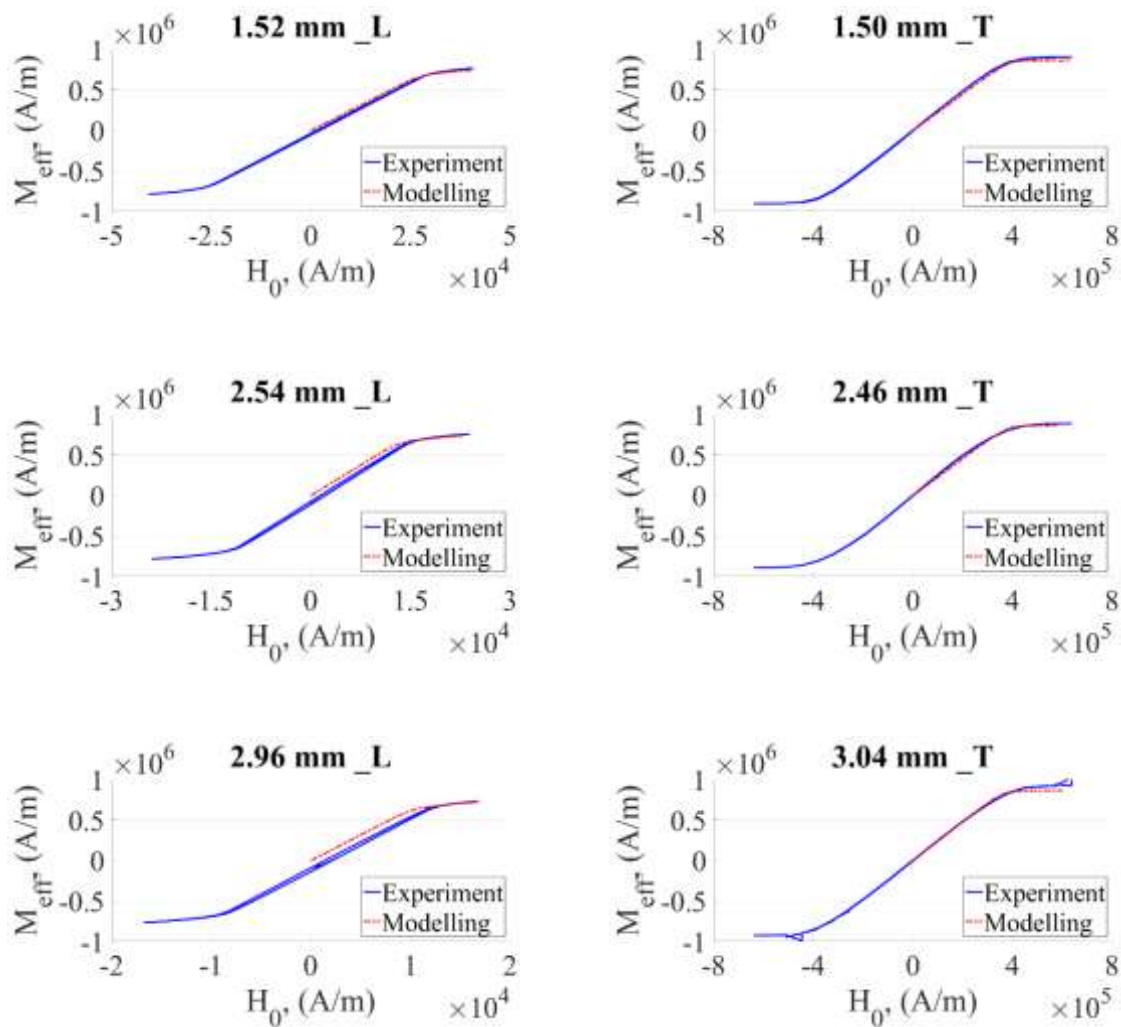


Figure S1. Comparison of experimental and modelling M-H curves of Ni/Fe pins with variable lengths (L: longitudinal, T: radial).

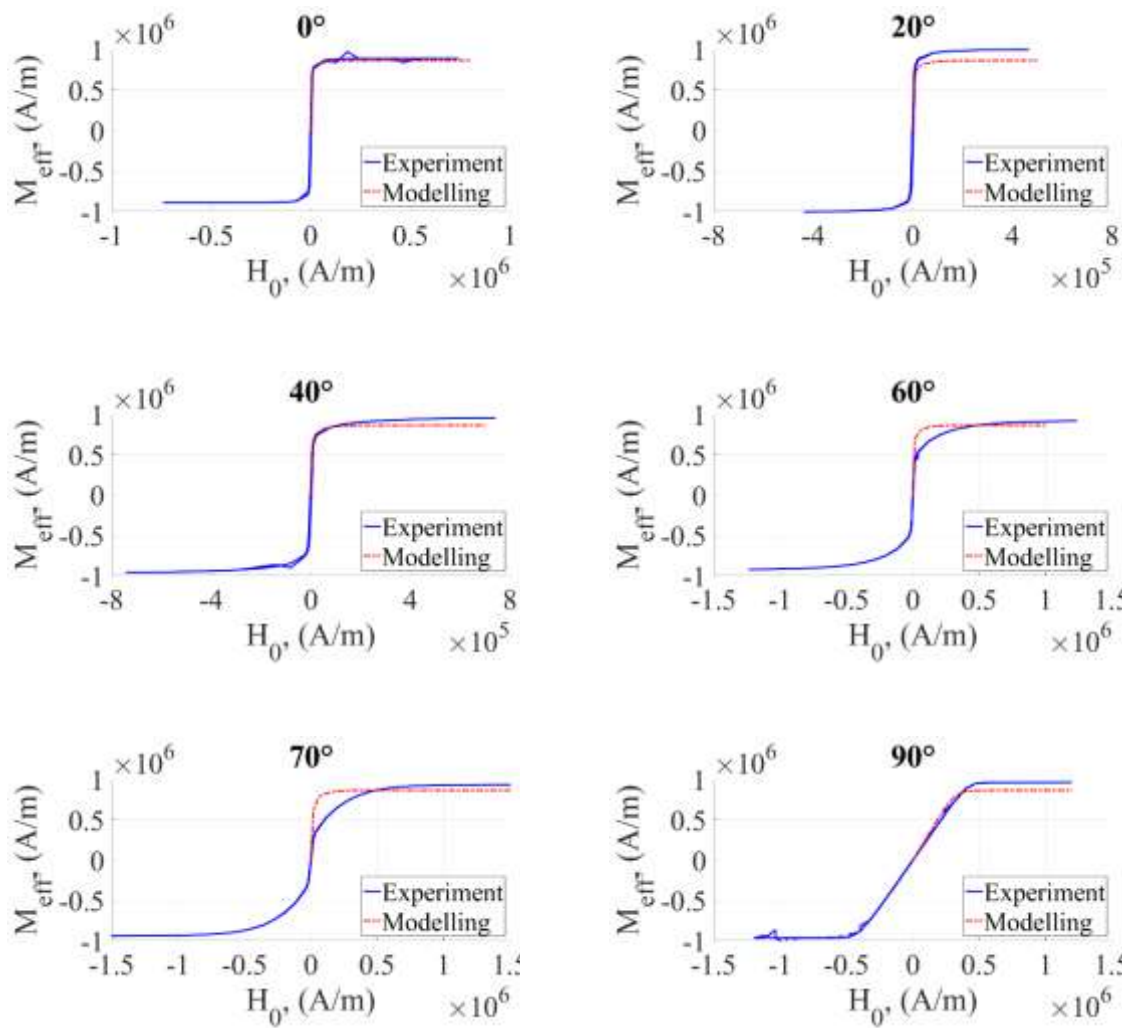


Figure S2. Comparison of experimental and modelling M-H curves of the single 4.05 mm long Ni/Fe alloy pin with variable inclination angles.

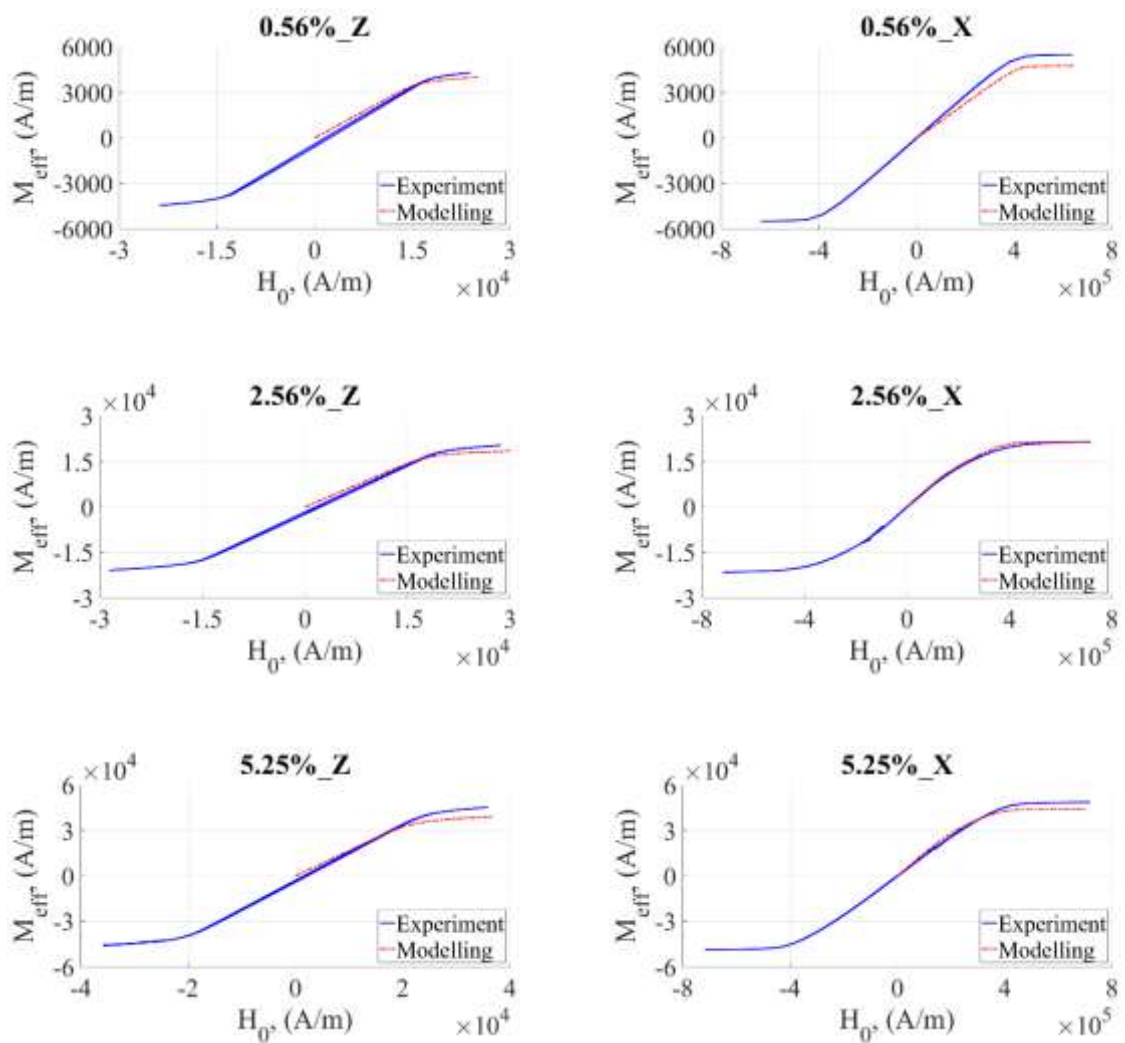


Figure S3. Comparison of experimental and modelling M-H curves of Ni/Fe pins reinforced laminate coupons (Z: out-of-plane, X: in-plane).